Available online at www.sciencedirect.com
ScienceDirect
Trans. Nonferrous Met. Soc. China 33(2023) 481−493
Transactions of Nonferrous Metals Society of China
www.tnmsc.cn

Thermo-physical simulation of deformation behavior and microstructure evolution for linear friction welding of near-β titanium alloy

Zhen-guo GUO[1], Tie-jun MA[1], Xia-wei YANG[1], Wen-ya LI[1], Jun TAO[2], Ju LI[2], Achilleas VAIRIS[1,3]

1. State Key Laboratory of Solidification Processing, Northwestern Polytechnical University, Xi'an 710072, China;
2. Aeronautical Key Laboratory for Welding and Joining Technologies, AVIC Manufacturing Technology Institute, Beijing 100024, China;
3. Mechanical Engineering Department, University of West Attica, Athens, 12241, Greece

Received 20 September 2021; accepted 22 December 2021

Abstract: In order to better understand the interface bonding behavior of linear friction welding (LFW) of a near-β titanium alloy, the thermo-physical simulation for deformation behavior and microstructure evolution of a near-β TB2 titanium alloy was carried out by using hot compression tests with specially designed hat-shaped specimens under different compression displacements, temperatures and strain rates which were decoupled in the simulation process. The results show that the peak shear stress in bonding zone (BZ) during hot compression increases with decreasing deformation temperature and increasing strain rate, and the width of BZ decreases with increasing deformation temperature and strain rate. The margin of BZ has largely deformed grains, and the center of BZ has fine equaxied recrystallized grains. The mechanism of the joint is continuous dynamic recrystallization (CDRX) and the degree of CDRX in BZ increases with increasing compression displacement, deformation temperature and strain rate. In addition, {112}[111] texture forms in the margin of BZ, and {110}[001] texture forms in the center of BZ.

Key words: linear friction welding; TB2 near-β titanium alloy; thermo-physical simulation; deformation behavior; microstructure evolution; microtexture evolution

1 Introduction

Solid-state welding is an excellent welding process for high strength alloys as it does not produce detrimental defects related to melting and solidification [1−3]. Linear friction welding (LFW) is a type of solid-state welding process emerged in the 1980s, which extends the application range of rotary friction welding and can be used to join non-axisymmetric cross-section metal components [4,5]. It is a key technology for manufacturing the integrally bladed discs (blisks) of high thrust-weight ratio aeroengines [5−7]. During welding, significant frictional heat is generated from the reciprocating movement of two components under friction pressure, which plasticizes the interfacial region. Subsequently, interfacial plastic metals are extruded under the combination of friction pressure and shear stress. When enough plastic metals are extruded, the forging pressure will be applied to completing welding. The LFW process is divided into four distinct stages: the initial, transition, equilibrium (quasi-steady friction stage) and deceleration [8−10]. The main features of LFW process are strong thermo-mechanical coupling, large temperature gradient, and local violent distortion [5]. To date, many materials have been successfully joined by LFW, such as titanium alloys [6−13], superalloys [14−16], steels [17−19],

Corresponding author: Tie-jun MA, Tel: +86-13709206759, E-mail: matiejun@nwpu.edu.cn;
Xia-wei YANG, Tel: +86-15829652047, E-mail: yangxiawei@nwpu.edu.cn
DOI: 10.1016/S1003-6326(22)66121-1

and aluminum alloys [20−22], where titanium alloys take up a great proportion.

LANG et al [23] investigated the LFWed TC11 two-phase titanium alloy joints and found that the grains in weld zone (WZ) were refined compared with those in base metal (BM), which indicated that dynamic recrystallization occurred in the WZ. The thermo-mechanically affected zone (TMAZ) was a highly deformed α+β microstructure along the friction direction. In addition, the grain size in WZ was greater with friction time rising. WANG et al [24] also studied the LFWed TC11 two-phase titanium alloy joints and identified that a micro-structure of recrystallized β grains with acicular α laths formed in WZ, and the grain size in WZ became smaller with increasing friction pressure. The grains in TMAZ were elongated along the friction direction and the width of the TMAZ reduced with friction pressure or/and shear velocity (calculated with $4\alpha f$ [5], α is the oscillation amplitude and f is the oscillation frequency). LI et al [6] found that if the friction pressure was relatively low, some spherical α grains formed near the weld interface of the LFWed TC11 two-phase titanium alloy joint. JI et al [25] investigated the LFWed Ti17 two-phase titanium alloy joint and found that the microstructure in WZ had the recrystallized β grains with a large number of parallel α needles which deposited along the grain boundaries, while in TMAZ, some partial recrystallized grains formed in severely deformed microstructures. LI et al [26] also identified dynamic recrystallization occurred in the WZ of LFWed Ti17 two-phase titanium alloy joint, and found that many superfine and equiaxed α grains dispersed uniformly in the recrystallized β grains or at the boundaries. In addition, highly deformed α and β phases were distributed along the friction direction in TMAZ. ROMERO et al [11] studied the influence of friction pressure on LFW of TC4 two-phase titanium alloy, and the results showed that the widths of WZ and TMAZ and the α-Ti intensity in WZ generally decreased with increasing the friction pressure. DALGAARD et al [12] carried out a LFW test of Ti5553 near-β titanium alloy and pointed out that the WZ was very fine β grains (1−5 μm) which were far smaller than the grains in BM (100−250 μm).

According to the above references, it can be stated that the weld microstructure of LFWed titanium alloy joints is changed compared with that of their BMs, and the weld microstructure of the same titanium alloy under various welding parameters shows different characteristics. When the LFW process enters the quasi-steady friction stage, the weld metals are in dynamic plastic deformation. The change of deformation conditions (e.g., strain rate, temperature and deformation amount) at this stage will affect the weld microstructure, which further affects the joint mechanical properties. The deformation conditions are affected by the LFW parameters (frequency, amplitude and friction pressure). However, the relationship between the deformation conditions and the welding parameters is complex. Hence, it is difficult to quantitatively study the effects of deformation conditions on weld microstructure by directly adjusting the welding parameters.

Thermo-physical simulation can be used to quantitatively investigate the effects of deformation conditions on the weld microstructure [27]. Our previous studies [27,28] simulated the flow behavior and interfacial microstructure evolution of the LFW of GH4169 superalloy by hot compression tests. However, only two cylindrical GH4169 superalloy specimens were upset with certain strain rates under axial forces and high temperatures. The interfacial metals were only deformed by extrusion, which did not well reflect the large shear deformation of the interfacial metals during LFW. Thus, in this work, the authors designed the special hat-shaped specimen which can generate shear deformation during hot compression tests, and used a near-β titanium alloy TB2 (Ti−5Mo−5V−8Cr−3Al) [29] whose phase structure is relatively simple and easy to identify the microstructure evolution after hot compression, to simulate the microstructure evolution of LFW with different deformation conditions.

2 Experimental

A commercially available TB2 near-β titanium alloy was used in this study. The nominal chemical composition of this alloy is listed in Table 1 [29]. The specimens were cut from a forged TB2 block, which was processed by solution aging treatment (solution treatment at 970 °C for 1 h with air cooling and aging treatment at 500 °C for 8 h with air cooling). As shown in Fig. 1, the equiaxed β grains

Table 1 Nominal chemical composition of TB2 alloy (wt.%) [29]

Al	Mo	V	Cr	Ti
2.5−3.5	4.7−5.7	4.7−5.7	7.5−8.5	Bal.

with random orientation appear in the BM of TB2, and the volume fraction of β phase in the BM is 99.3%. The grain boundaries in the BM are mainly high-angle grain boundaries (HAGBs, the black lines in Fig. 1(b)), and only a small number of low-angle grain boundaries (LAGBs, the white lines in Fig. 1(b)) are inside the equiaxed grains. The β-transus temperature and recrystallization temperature of TB2 are about 750 and 483 °C, respectively [29].

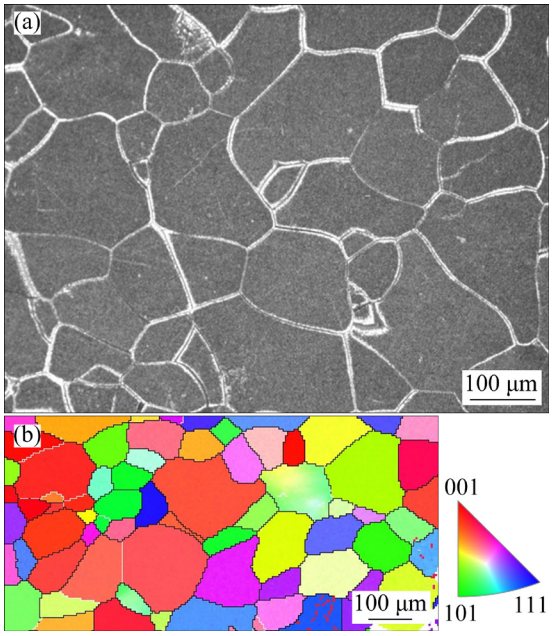

Fig. 1 BM of used TB2 titanium alloy: (a) Optical microstructure; (b) Inverse pole figure (IPF)

The hat-shaped hot compression specimens were designed by referring the specimen structures in some shear deformation studies of alloys [30−32]. The dimensions and configuration of the hat-shaped specimens are shown in Fig. 2. Figure 3 shows the schematic diagrams of the hot compression test with the hat-shaped specimen. During the hot compression, the cylinder was pressed into the ring at a certain strain rate under an axial force, and large shear deformation occurred at the connection position between the ring and the cylinder to form a weld like bonding zone. The hot compression tests were conducted on a Gleeble−3500 thermal simulator (the maximum heating rate reached 10000 °C/s, the temperature control accuracy reached ±1 °C; the maximum tensile and compressive loads were 100 kN; the displacement measurement accuracy was 0.002 mm).

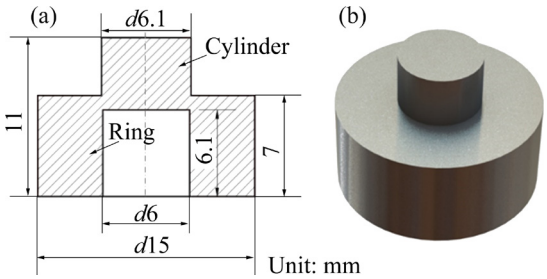

Fig. 2 Dimensions (a) and configuration (b) of designed hat-shaped specimens

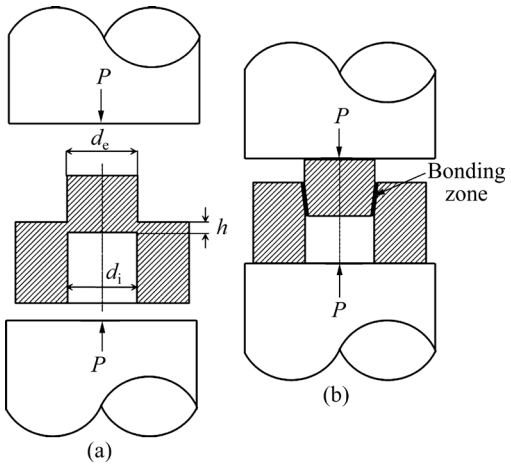

Fig. 3 Schematic diagrams of hot compression test: (a) Before compression; (b) After compression

The hot compression tests were conducted at various compression displacements, strain rates and temperatures as listed in Table 2. The compression displacements were 1, 2, and 3.6 mm, respectively. Referring to the interfacial strain rate equation during LFW developed by VAIRIS and FROST [8−10] and the numerical simulation results given in reference [33], two typical strain rates of 1 and 10 s^{-1} were selected for the hot compression tests. The equation is as follows:

$$\dot{\varepsilon} = \alpha f / L \tag{1}$$

where $\dot{\varepsilon}$ is the interfacial metals strain rate (s^{-1}), α is the oscillation amplitude (mm), f is the oscillation frequency (Hz), and L is the length of the specimen along the friction direction (mm). The temperatures selected in this study are 650 and 850 °C, which are below and above the β-transus temperature of TB2, respectively.

Table 2 Process parameters of hot compression tests

Specimen	Temperature/°C	Strain rate/s^{-1}	Compression displacement/mm	Heating rate/ (°C·s^{-1})	Holding time/min	Cooling method
1#	850	1	1	10	3	Air cooling
2#	850	1	2			
3#	850	1	3.6			
4#	650	1	3.6			
5#	650	10	3.6			
6#	850	10	3.6			

After the hot compression tests, the polished metallographic specimens were etched using Kroll's reagent (0.5 vol.% HF + 1.5 vol.% HNO_3 + 2 vol.% HCl + 96 vol.% H_2O). Subsequently, the specimens were observed under an optical microscope (OM) (OLYMPUS PMG3) and a scanning electron microscope (SEM) (Helios G4 CX) to investigate the microstructure characteristics of the hot compression bonded joints. The electron back-scattered diffraction (EBSD) analysis was also carried out to investigate the microstructure evolution of the hot compression bonded joints. The samples were electro-polished in a solution (30 vol.% C_4H_9OH + 64 vol.% CH_3OH + 6 vol.% $HClO_4$) with a voltage of 20 V for 80 s at 0 °C firstly. And then, the EBSD was performed on a SEM (TESCAN MIRA3 XMU) with an Oxford EBSD data acquisition software (HKL-Channel 5). Moreover, the Vickers hardness of hot compression bonded TB2 joint was tested using an HX−1000 hardness tester. The test directions were along and perpendicular to the bonding zone (BZ). The load was 1 kg, the dwell time was 10 s, and the test step length was 150 μm.

3 Results and discussion

3.1 Deformation behaviors of hot compression bonded joints under different conditions

The cross-sections of 1#, 2# and 3# joints under different compression displacements are shown in Figs. 4(a, c, e), respectively. It can be seen from Figs. 4(a, c, e) that when the temperature and strain rate are constant, with the increase of compression displacement, the deformation degree of interfacial metal between the cylinder and ring increases. Figure 4(b) shows that when the compression displacement is 1 mm, the BZ is mainly composed of largely deformed grains. When the compression displacement is 2 mm, a shear band forms in the BZ, and a few fine equiaxed grains form at the largely deformed grain boundaries (marked by arrows in Fig. 4(d)), which indicates that local dynamic recrystallization occurs. When the compression displacement is 3.6 mm, there are a large number of fine equiaxed grains distributing in the BZ (Fig. 4(f)), which indicates that the sufficient dynamic recrystallization occurs. Based on the above results, it can be concluded that with the increase of compression displacement, the dynamic recrystallization degree of the BZ in the hot compression bonded joint increases. Generally, in most LFWed titanium alloy joints, dynamic recrystallization occurs in the weld zone, resulting in forming many fine equiaxed recrystallized grains. Hence, when the compression displacement is 3.6 mm, the microstructure of the BZ is similar to the weld zone of a LFWed joint.

During the hot compression tests, the shear stress of the BZ can be expressed as follows [32]:

$$\tau = P / \left[\pi h \left(\frac{d_e + d_i}{2} \right) \right] \tag{2}$$

where τ is the shear stress (MPa), P is the axial force (MPa), h is the initial connection height between the ring and the cylinder of the specimen (mm), d_e and d_i are the diameter of the cylinder and the inner diameter of the ring (mm), respectively (see Fig. 3). Based on the recorded axial forces, the shear stresses were calculated with Eq. (2). Figure 5 shows the shear stress−displacement curves of 1#, 2#, and 3# joints under different compression displacements. It should be pointed out that the pre-set compression displacements of the three joints are 1, 2, and 3.6 mm, respectively, but the final displacements in Fig. 5 are less than them. This is because slight displacement occurs during the holding time before the compression, and the

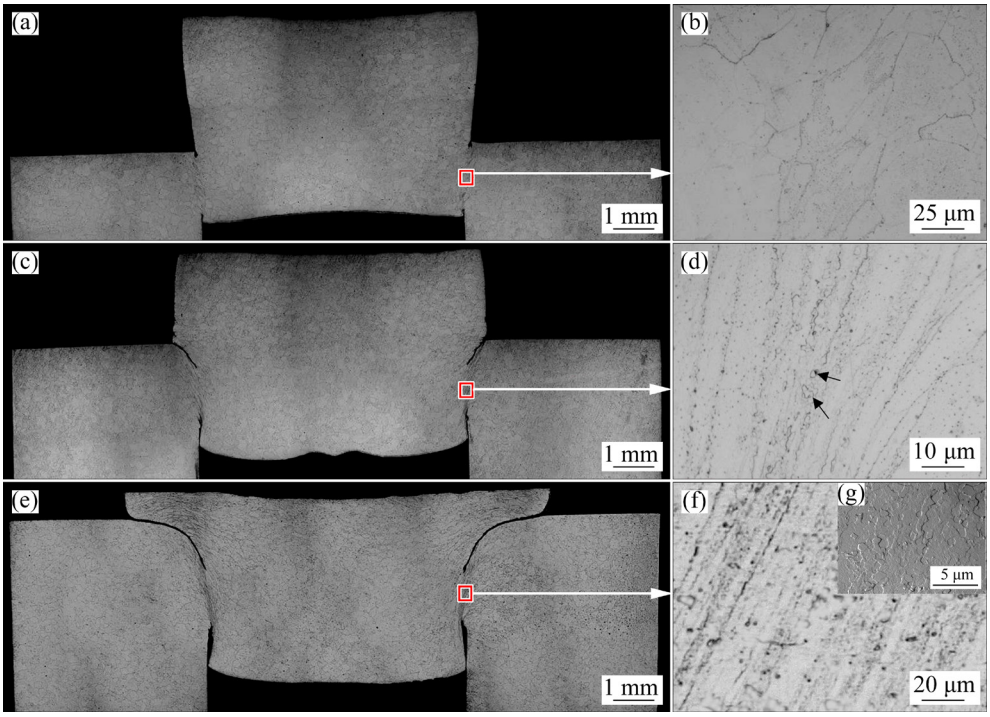

Fig. 4 Cross-sectional micrographs of 1#, 2# and 3# joints at different compression displacements: (a) Cross-section of 1# joint; (b) BZ of 1# joint (red frame in (a)); (c) Cross-section of 2# joint; (d) BZ of 2# joint (red frame in (c)); (e) Cross-section of 3# joint; (f) BZ of 3# joint (red frame in (e)); (g) High magnification of (f) by SEM

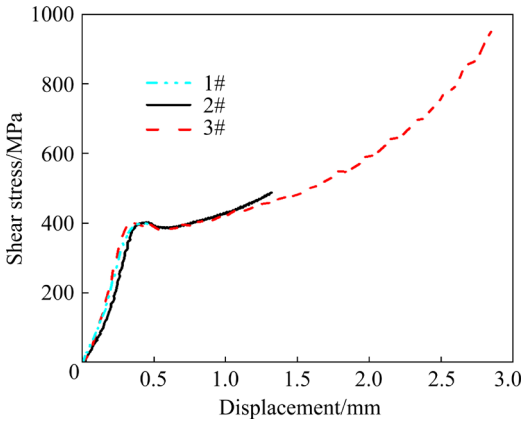

Fig. 5 Shear stress−displacement curves of 1#, 2# and 3# joints

displacements in Fig. 5 are the actual compression displacements of the three joints. At the initial stage of the hot compression, the shear stresses of the three joints increase rapidly. When the displacement reaches about 0.4 mm, there is a shear stress peak (about 400 MPa). When the displacement is larger than 0.4 mm, the shear stresses of 2# and 3# joints begin to decrease. It can be attributed to that dynamic recrystallization occurs when the accumulated dislocation density exceeds a critical strain [34]. It should be pointed out that the shear stress curves of 2# and 3# joints do not show wavy change when the compression displacement is larger than 0.4 mm, which illustrates that the dynamic recrystallization mechanism of the hot compression bonded TB2 joint is continuous dynamic recrystallization (CDRX) [35]. Moreover, the shear stresses of 2# and 3# joints increase continuously after the shear stress valley of about 380 MPa, which can be attributed to that the large diameter cylinder is continuously pressed into the small inner diameter ring.

The shear stress−displacement curves of 3#, 4#, 5# and 6# joints are shown in Fig. 6. When the strain rate is 1 s^{-1}, the peak shear stress of 3# joint (400 MPa) is lower than that of 4# joint (590 MPa). When the strain rate is 10 s^{-1}, the peak shear stress of 6# joint (530 MPa) is lower than that of 5# joint (660 MPa). This can be attributed to that the deformation temperatures of 3# and 6# joints (850 °C) are higher than those of 4# and 5# joints (650 °C), the deformation resistances of 3# and 6# joints are lower than those of 4# and 5# joints during hot compression, leading to the fact that the applied axial forces of 3# and 6# joints are lower than those of 4# and 5# joints. Hence, according to

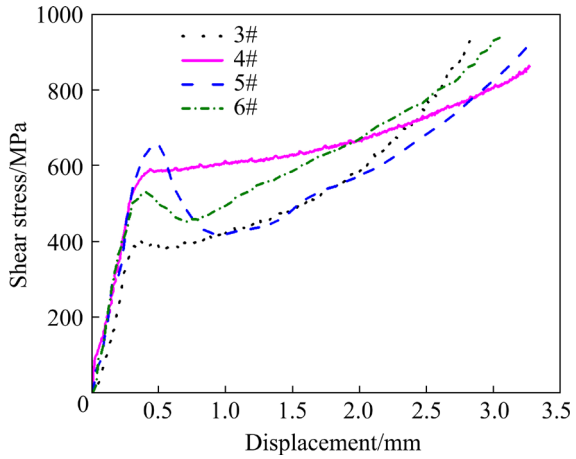

Fig. 6 Shear stress−displacement curves of 3#, 4#, 5# and 6# joints

Eq. (2), the peak shear stresses of 3# and 6# joints are lower. When the deformation temperature is 850 °C, the peak shear stress of 3# joint is lower than that of 6# joint. When the deformation temperature is 650 °C, the peak shear stress of 4# joint is lower than that of 5# joint. This can be attributed to that the strain rates of 3# and 4# joints (1 s^{-1}) are lower than those of 5# and 6# joints (10 s^{-1}). When the strain rate is relatively high during hot compression, more dislocations are driven at per unit time and more serious dislocation tangling forms, which causes larger degree work hardening and higher peak shear stress [27,28].

The shear stresses of 3#, 5# and 6# joints decrease obviously after the peak shear stress due to the dynamic recrystallization. However, the shear stress of the 4# joint does not decrease obviously, indicating that there is no dynamic recrystallization occurring during hot compression or the dynamic recrystallization is not obvious. It should be attributed to the lower deformation temperature and strain rate of 4# joint. After reaching the peak shear stress, the shear stresses of 5# and 6# joints decrease more obviously than those of 3# and 4# joints. This is because more distortion energy is stored in 5# and 6# joints due to their higher strain rates, and larger degree dynamic recrystallization occurs. In addition, the shear stress of 3# joint decreases more obviously than that of 4# joint after reaching the peak shear stress. This is because the degree of dynamic recrystallization increases with increasing deformation temperature. However, the shear stress of 5# joint shows the more obvious drop than that of 6# joint after the peak shear stress, although the deformation temperature of 5# joint is lower than that of 6# joint, which can be attributed to that the BZ of 5# joint breaks, as shown in Fig. 7. And the reason why the BZ of 5# joint breaks is that the shear strength of TB2 titanium alloy at 650 °C is lower than 640 MPa [29], but the peak shear stress in the BZ of 5# joint during hot compression reaches 660 MPa due to the lower deformation temperature (650 °C) and higher strain rate (10 s^{-1}).

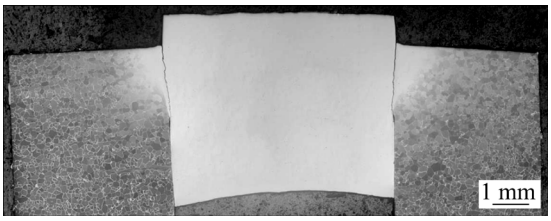

Fig. 7 Cross-sectional micrograph of 5# joint

Based on the aforementioned results, it can be concluded that the peak shear stress during the hot compression of TB2 titanium alloy increases with decreasing deformation temperature and increasing strain rate. And the dynamic recrystallization degree in the BZ of hot compression bonded TB2 joint increases with increasing deformation temperature and strain rate.

The microstructures of the BZs in 3#, 4# and 6# joints are shown in Fig. 8. In previous description, the dynamic recrystallization occurs in the BZs of 3# and 6# joints, so the grains in the BZs of 3# and 6# joints are refined, as shown in Figs. 8(a) and (c), respectively. It can be seen from Fig. 8(b) that the grains in the BZ of 4# joint are mainly deformed grains and the microstructure shows streamline characteristic. This is because the dynamic recrystallization does not occur or the dynamic recrystallization is not obvious in the BZ of 4# joint, and the grains are not refined. The width of the BZ in 3# joint is about 180 μm and it is smaller than that of the BZ in 4# joint (240 μm). It can be attributed to that the deformation temperature of 4# joint (650 °C) is lower that of 3# joint (850 °C), and the softening degree of the BZ metal of 4# joint is less than that of 3# joint during hot compression, so the BZ metal of 4# joint is relatively difficult to flow along the shear direction, resulting in forming the wider BZ. Although the deformation temperatures of 3# and 6# joints are both 850 °C, the width of the BZ in 6#

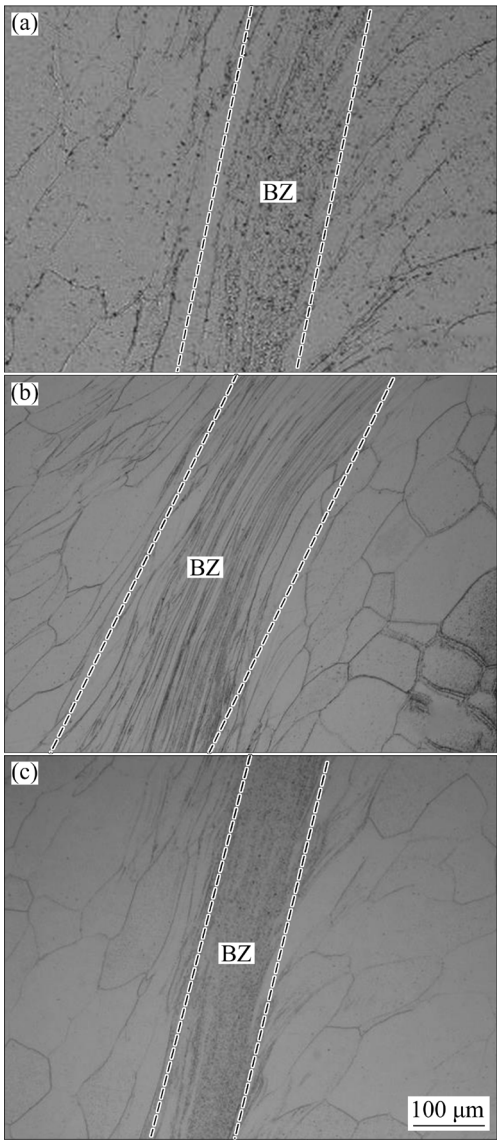

Fig. 8 OM images of BZs in 3#, 4# and 6# joints: (a) 3# joint; (b) 4# joint; (c) 6# joint

joint is about 115 μm, which is smaller than that of 3# joint. It can be attributed to that the shear stress of 6# joint is larger than that of 3# joint during hot compression (see Fig. 6), so the BZ metal of 6# joint is easier to flow along the shear direction, resulting in forming the narrower BZ. Hence, it can be concluded that the width of BZ in the hot compression bonded TB2 joint decreases with increasing deformation temperature and strain rate.

3.2 Microstructure evolution of hot compression bonded joint

The 6# joint is selected to conduct the EBSD test to observe the microstructure evolution of the BZ in hot compression bonded TB2 joint. Except for the BM, four positions are scanned, which are shown in Fig. 9. Position *A* is located at the margin of BZ, and Position *D* is located at the center of BZ.

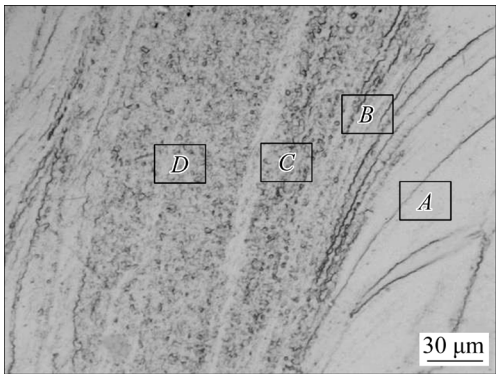

Fig. 9 Positions of EBSD scanning

Figure 10 shows the IPFs of Positions *A*, *B*, *C* and *D* in Fig. 9. The white lines represent LAGBs with the misorientation angles of 2°−15°, and the black lines represent HAGBs with the misorientation angle greater than 15°. Figure 10(a) shows that the grains at Position *A* are mainly elongated grains, which form from the BM equiaxed grains under strong thermo-mechanical coupling during the hot compression. Some LAGBs form in the elongated grains. This is because a large number of dislocations gather in the elongated grains during hot compression, and dislocations rearrangement occurs to form some LAGBs [24]. Figure 10(b) shows that the elongated grains are still in Position *B*, and the LAGBs in this position are more than those in Position *A*. There are many sub-structure grains which are composed of LAGBs forming in the elongated grains, and some sub-structure grains transform to equiaxed recrystallized grains (marked by arrows in Fig. 10(b)) which are composed of HAGBs by absorbing dislocations. This reveals that the low degree dynamic recrystallization occurs at Position *B*. Figure 10(c) shows that at Position *C*, there are many fine equiaxed recrystallized grains and sub-structure grains, with no elongated grains. This reveals that sufficient dynamic recrystallization occurs in this position. As shown in Fig. 10(d), Position *D* also has many fine equiaxed recrystallized grains, but the average grain size (4.5 μm) is larger than that at Position *C* (2.5 μm). It can be attributed to that the temperature of Position *D* is higher than that of Position *C* during hot compression due to more

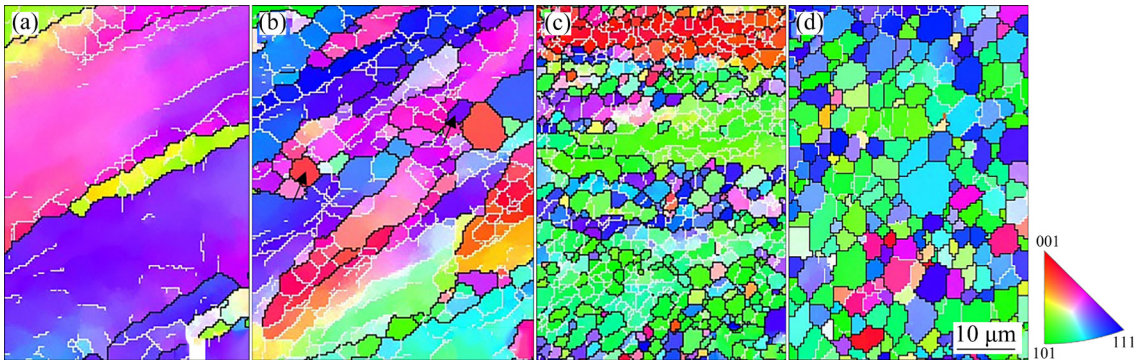

Fig. 10 IPFs of Positions *A*, *B*, *C* and *D* in Fig. 9: (a) Position *A*; (b) Position *B*; (c) Position *C*; (d) Position *D*

plastic deformation heat, so the recrystallized grains at Position *D* grow up. From above results, it can be stated that from Position *A* to Position *D*, largely deformed grains transform to equiaxed recrystallized grains, and dynamic recrystallization degree increases gradually. There is a similar rule in LFWed titanium alloy joints, from thermo-mechanically affected zone to weld zone, deformed grains transform to equiaxed recrystallized grains and the degree of dynamic recrystallization increases. Besides, it should be pointed out that there are a large number of LAGBs and sub-structure grains forming in the hot compression bonded TB2 joint during hot compression, which is a significant characteristic of continuous dynamic recrystallization (CDRX) [36]. Hence, the dynamic recrystallization mechanism of the hot compression bonded TB2 joint is CDRX, which confirms the conclusion in Section 3.1. Figure 11 shows that the average misorientation angles of Positions *A*, *B*, *C* and *D* in Fig. 9 are 17.6°, 19.3°, 26.5° and 32.0°, respectively, which illustrates that proportion of HAGBs increases from Position *A* to Position *D*. It can be attributed to that the degree of CDRX increases from Position *A* to Position *D* and the number of LAGBs transforming into HAGBs increases.

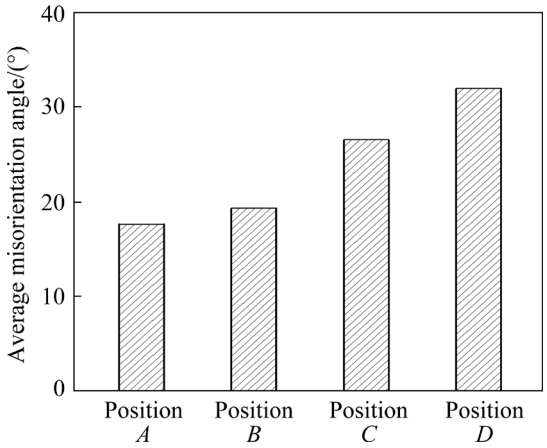

Fig. 11 Average misorientation angles of Positions *A*, *B*, *C* and *D* in Fig. 9

3.3 Microtexture evolution of hot compression bonded joint

Figure 12 shows the {100}, {110} and {111} pole figures of different positions (the BM and Position *A*, *B*, *C* and *D* in Fig. 9) of 6# joint. The X_0 direction represents the shear direction, and the Y_0 direction represents the shear plane normal. The evolution of the texture is described using the density of pole figures given as multiple of uniform uniform distribution (mud). The deformation mode of the hot compression in this research can be regarded as simple shear. For a bcc material, seven ideal textures in simple shear are identified [37−39], which are given in Fig. 13 and Table 3. From Fig. 12(a), it is evident that F texture ({110}[001]) which forms in forging process dominates in BM and the maximum texture density is about 8.52 mud. It can be seen from Fig. 12(b) that D_2 texture ($\{11\bar{2}\}[111]$) dominates at Position *A* and the maximum texture density is about 16.57 mud. The texture density of Position *A* is larger than that of the BM because the grains at Position *A* deform along the shear direction under strong shear stress. Figures 12(c) and (d) reveal that D_1 texture ($\{\bar{1}\,\bar{1}2\}[111]$) dominates at Positions *B* and *C*, and the maximum texture densities are 8.78 and8.99 mud, respectively. Both of them are lower than that of Position *A*, which can be attributed to that dynamic recrystallization occurs at Positions *B* and *C*, and the recrystallized grain orientations at

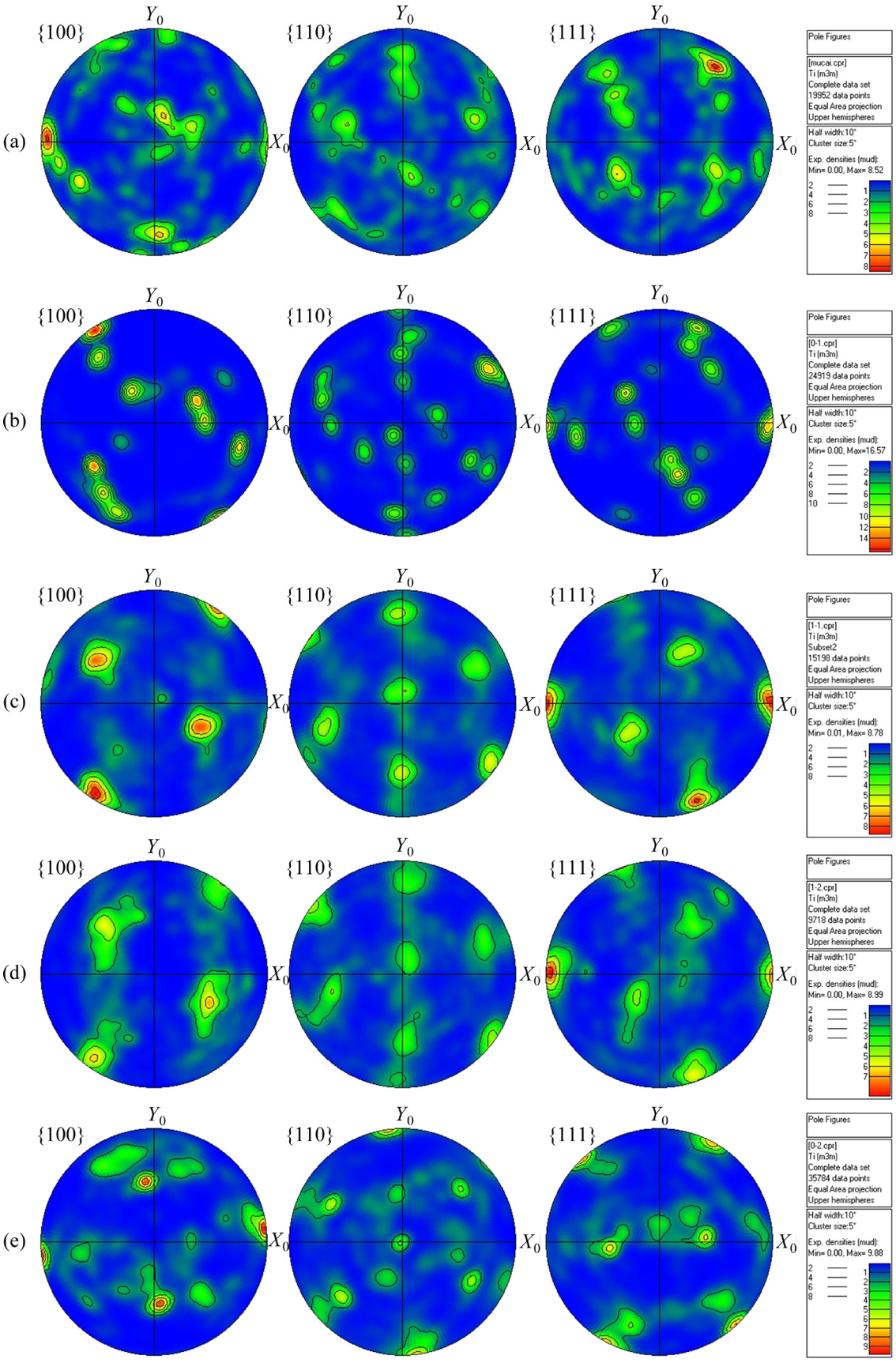

Fig. 12 Pole figures of 6# joint at different positions in Fig. 9: (a) BM; (b) Position *A*; (c) Position *B*; (d) Position *C*; (e) Position *D*

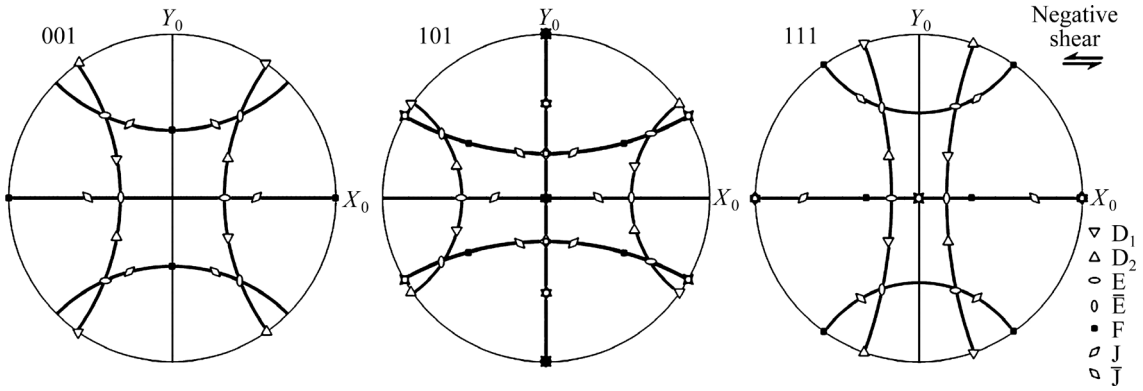

Fig. 13 Ideal crystallographic orientations of bcc material in simple shear [37−39]

Table 3 Ideal crystallographic orientations of bcc material in simple shear [37−39]

Texture	Description
D_1	$\{\bar{1}\,\bar{1}2\}[111]$
D_2	$\{11\bar{2}\}[111]$
E	$\{110\}[1\,\bar{1}1]$
$\bar{E}$	$\{110\}[\bar{1}1\,\bar{1}]$
F	$\{110\}[001]$
J	$\{110\}[1\,\bar{1}2]$
$\bar{J}$	$\{110\}[\bar{1}1\bar{2}]$

Positions *B* and *C* tend to be more disperse. Moreover, it should be pointed out that the D_1 and D_2 textures are mirror-symmetric and both of them belong to {112}[111] texture. This type of texture has also been found in the LFWed TB9 near-*β* titanium alloy joint [40] and LFWed TC11 two-phase titanium alloy joint [24]. Figure 12(e) shows that F texture ({110}[001]) dominates at Position *D* and the maximum texture density is 9.88 mud. Although sufficient CDRX occurs at Position *D*, the texture density is still larger than that of Positions *B* and *C*, which can be attributed to that Position *D* is the most plastic zone of the hot compression bonded TB2 joint, the strong shear stress contributes to the recrystallized grains rotation and the F texture forms in the center of BZ.

3.4 Microhardness of hot compression bonded joint

Figure 14 shows positions of the micro-hardness measurement on the cross-section of 6# joint, where Line *A* is perpendicular to the shear direction and Line *B* is along the shear direction. Figure 15(a) shows the microhardness distribution along Line *A*, and there is a microhardness peak of about HV 310, which is located at the center of BZ. It can be seen from Fig. 15(b) that the microhardness of the center of BZ along Line *B* is a little uniform, and the average microhardness is HV 314, which is higher than the average microhardness of BM (HV 278). Because the grains in the center of BZ are refined compared with the grains in BM due to dynamic recrystallization, the fine grain strengthening makes the microhardness of the center of BZ higher than that of BM. In addition, it can be seen from Fig. 15(a) that the average microhardness of the margin of BZ (HV 285) is also higher than that of BM, which can be attributed to the deformed grains along the shear direction, causing the strain strengthening. In the study on LFW of TB2 titanium alloy, it was found that the fine grain strengthening in weld zone and the strain strengthening in the thermo-mechanically affected zone make its microhardness higher than that of BM [41,42]. Hence, the microstructure evolution and strengthening mechanism of the hot compression bonded TB2 joint are similar to those of the LFWed TB2 titanium alloy joint.

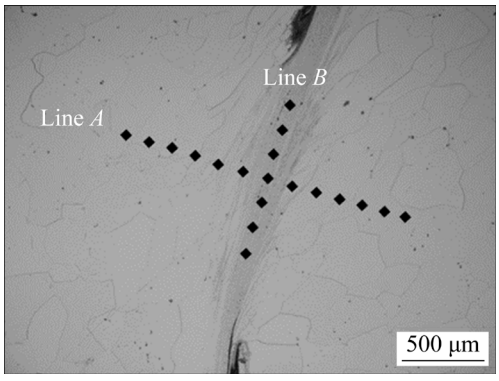

Fig. 14 Microhardness measurement positions of 6# joint

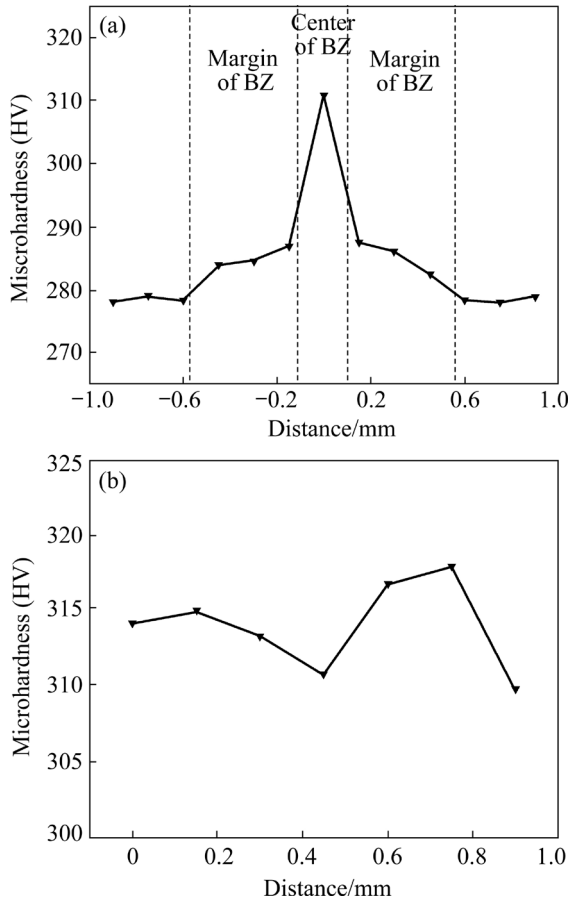

Fig. 15 Microhardness distributions of 6# joint: (a) Perpendicular to shear direction (Line *A*); (b) Along shear direction (Line *B*)

4 Conclusions

(1) The shear stress−displacement curves of the hot compression tests are sensitive to the strain rate and temperature. Under the same compression displacement, the peak shear stress increases with decreasing temperature and/or increasing strain rate.

(2) The dynamic recrystallization mode of the BZ in hot compression bonded TB2 joints is CDRX, and the degree of CDRX increases with increasing compression displacement, temperature and strain rate.

(3) When the compression displacement is 3.6 mm and the strain rate is 1 s^{-1}, the width of BZ decreases from 240 to 180 μm with the temperature increasing from 650 to 850 °C. When the compression displacement is 3.6 mm and the temperature is 850 °C, the width of BZ decreases from 180 to 115 μm with the strain rate increasing from 1 to 10 s^{-1}.

(4) From the margin of BZ to the center of BZ, largely deformed grains transform to fine recrystallized grains, and the degree of CDRX increases. The {112}[111] texture forms in the margin of BZ and the maximum texture density is 16.57 mud; the {110}[001] texture forms in the center of BZ and the maximum texture density is only 9.88 mud due to CDRX occurring.

(5) The average microhardnesses of the center and margin of BZ are HV 314 and HV 285, respectively. Both of them are higher than that of BM (HV 278), which can be attributed to the fine grain strengthening in the center of BZ and the strain strengthening in the margin of BZ.

Acknowledgments

This work was supported by the National Natural Science Foundation of China (Nos. 51675435, 51875470, 52074228), and the Research Fund of the State Key Laboratory of Solidification Processing (NPU), China (No. 2021-TZ-01, 2021-TS-07).

References

[1] GENG Pei-hao, QIN Guo-liang, ZHOU Jun, LI Chang-an. Parametric optimization and microstructural characterization of friction welded aeronautic aluminum alloy 2024 [J]. Transactions of Nonferrous Metals Society of China, 2019, 29: 2483−2495.

[2] ZHANG Chuan-chen, ZHANG Tian-cang, JI Ya-juan, HUANG Ji-hua. Effects of heat treatment on microstructure and microhardness of linear friction welded dissimilar Ti alloys [J]. Transactions of Nonferrous Metals Society of China, 2013, 23: 3540−3544.

[3] KUMAR R, BALASUBRAMANIAN M. Application of response surface methodology to optimize process parameters in friction welding of Ti−6Al−4V and SS304L rods [J]. Transactions of Nonferrous Metals Society of China, 2015, 25: 3625−3633.

[4] MCANDREW A R, COLEGROVE P A, BÜHR C, FLIPO B C D, VAIRIS A. A literature review of Ti−6Al−4V linear friction welding [J]. Progress in Materials Science, 2018, 92: 225−257.

[5] LI Wen-ya, VAIRIS A, PREUSS M, MA Tie-jun. Linear and rotary friction welding review [J]. International Materials Reviews, 2016, 61: 71−100.

[6] LI Wen-ya, SUO Juan-di, MA Tie-jun, FENG Yan, KIM K. Abnormal microstructure in the weld zone of linear friction welded Ti−6.5Al−3.5Mo−1.5Zr−0.3Si titanium alloy joint and its influence on joint properties [J]. Materials Science and Engineering A, 2014, 599: 38−45.

[7] MA Tie-jun, CHEN Tao, LI Wen-ya, WANG Shi-wei, YANG Si-qian. Formation mechanism of linear friction welded Ti−6Al−4V alloy joint based on microstructure observation [J]. Materials Characterization, 2011, 62: 130−135.

[8] VAIRIS A, FROST M. High frequency linear friction welding of a titanium alloy [J]. Wear, 1998, 217: 117−131.

[9] VAIRIS A, FROST M. On the extrusion stage of linear friction welding of Ti−6Al−4V [J]. Materials Science and Engineering A, 1999, 271: 477−484.

[10] VAIRIS A, FROST M. Modelling the linear friction welding of titanium blocks [J]. Materials Science and Engineering A, 2000, 292: 8−17.

[11] ROMERO J, ATTALLAH M M, PREUSS M, KARADGE M, BRAY S E. Effect of the forging pressure on the microstructure and residual stress development in Ti−6Al−4V linear friction welds [J]. Acta Materialia, 2009, 57: 5582−5592.

[12] DALGAARD E, WANJARA P, GHOLIPOUR J, CAO X, JONAS J J. Linear friction welding of a near-β titanium alloy [J]. Acta Materialia, 2012, 60: 770−780.

[13] WANG Xin-yu, LI Wen-ya, MA Tie-jun, VAIRIS A. Characterisation studies of linear friction welded titanium joints [J]. Materials and Design, 2017, 116: 115−126.

[14] KARADGE M, PREUSS M, WITHERS P J, BRAY S. Importance of crystal orientation in linear friction joining of single crystal to polycrystalline nickel-based superalloys [J]. Materials Science and Engineering A, 2008, 491: 446−453.

[15] CHAMANFAR A, JAHAZI M, GHOLIPOUR J, WANJARA P, YUE S. Analysis of integrity and microstructure of linear friction welded Waspaloy [J]. Materials Characterization, 2015, 104: 149−161.

[16] MA Tie-jun, CHEN Xi, LI Wen-ya, YANG Xia-wei, ZHANG Yong, YANG Si-qian. Microstructure and mechanical property of linear friction welded nickel-based superalloy joint [J]. Materials and Design, 2016, 89: 85−93.

[17] LI Yan-mo, LIU Yong-chang, LIU Chen-xi, MA Zong-qing, HUANG Yuan, WANG Zu-min, LI Wen-ya. Microstructure evolution and mechanical properties of linear friction welded S31042 heat-resistant steel [J]. Journal of Materials Science & Technology, 2018, 34: 653−659.

[18] SU Yu, LI Wen-ya, WANG Xin-yu, MA Tie-jun, MA Liang, DOU Xiao-mu. The sensitivity analysis of microstructure and mechanical properties to welding parameters for linear friction welded rail steel joints [J]. Materials Science and Engineering A, 2019, 764: 138251.

[19] KELLY M R, SCHMID S R, ADAMS D C, FLETCHER J, HEARD R. Experimental investigation of linear friction welding of AISI 1020 steel with pre-heating [J]. Journal of Manufacturing Processes, 2019, 39: 26−39.

[20] ROTUNDO F, MARCONI A, MORRI A, CESCHINI A. Dissimilar linear friction welding between a SiC particle reinforced aluminum composite and a monolithic aluminum alloy: Microstructural, tensile and fatigue properties [J]. Materials Science and Engineering A, 2013, 559: 852−860.

[21] LIS A, MOGAMI H, MATSUDA T, SANO T, YOSHIDA R, HORI H, HIROSE A. Hardening and softening effects in aluminium alloys during high-frequency linear friction welding [J]. Journal of Materials Processing Technology, 2018, 255: 547−558.

[22] MOGAMI H, MATSUDA T, SANO T, YOSHIDA R, HORI H, HIROSE A. High-frequency linear friction welding of aluminum alloys [J]. Materials & Design, 2018, 139: 457−466.

[23] LANG Bo, ZHANG Tian-cang, LI Xiao-hong, GUO De-lun. Microstructural evolution of a TC11 titanium alloy during linear friction welding [J]. Journal of Materials Science, 2010, 45: 6218−6224.

[24] WANG Xin-yu, LI Wen-ya, MA Tie-jun, YANG Xia-wei, VAIRIS A. Effect of welding parameters on the microstructure and mechanical properties of linear friction welded Ti−6.5Al−3.5Mo−1.5Zr−0.3Si joints [J]. Journal of Manufacturing Processes, 2019, 46: 100−108.

[25] JI Ying-ping, CHAI Zhen-zhen, ZHAO Da-long, WU Su-jun. Linear friction welding of Ti−5Al−2Sn−2Zr−4Mo−4Cr alloy with dissimilar microstructure [J]. Journal of Materials Processing Technology, 2014, 214: 979−987.

[26] LI Wen-ya, MA Tie-jun, YANG Si-qian. Microstructure evolution and mechanical properties of linear friction welded Ti−5Al−2Sn−2Zr−4Mo−4Cr (Ti17) titanium alloy joints [J]. Advanced Engineering Materials, 2010, 12: 35−43.

[27] YANG Xia-wei, LI Wen-ya, MA Tie-jun, HU Shi-tian, HE Yong, LI Long, XIAO Bo. Thermo-physical simulation of the compression testing for constitutive modeling of GH4169 superalloy during linear friction welding [J]. Journal of Alloys and Compounds, 2016, 656: 395−407.

[28] YANG Xia-wei, LI Wen-ya, FENG Yan, YU Si-qi, XIAO Bo. Physical simulation of interfacial microstructure evolution for hot compression bonding behavior in linear friction welded joints of GH4169 superalloy [J]. Materials and Design, 2016, 104: 436−452.

[29] Editorial Board of China Aeronautical Materials Handbook. China aeronautical materials handbook [M]. 2nd ed. Beijing: Standards Press of China, 2001. (in Chinese)

[30] NEMAT-NASSER S, ISAACS J B, LIU M Q. Microstructure of high-strain, high-strain rate deformed tantalum [J]. Acta Materialia, 1998, 46: 1307−1325.

[31] KAD B K, GEBERT J M, PEREZ-PRADO M T, KASSNER M E, MEYERS M A. Ultrafine-grain-sized zirconium by dynamic deformation [J]. Acta Materialia, 2006, 54: 4111−4127.

[32] MEYERS M A, SUBHASH G, KAD B K, PRASSAD L. Evolution of microstructure and shear-band formation in α-hcp titanium [J]. Mechanics of Materials, 1994, 17: 175−193.

[33] ZHAO Peng-kang, FU Li, ZHONG De-chao. Numerical simulation of transient temperature and axial deformation during linear friction welding between TC11 and TC17 titanium alloys [J]. Computational Materials Science, 2014, 92: 325−333.

[34] SUN Ya-li, LIU Qing-cai, HUANG Xin, ZHANG Fa-qing, YANG Jian, MEI Hua. Effect of jet milling on micro-strain behavior and rupture behavior of agglomerates of ultrafine WC powders [J]. Transactions of Nonferrous Metals Society of China, 2019, 29: 2128−2140.

[35] CAO Jun, LI Fu-guo, MA Xin-kai, SUN Zhan-kun. Tensile stress-strain behavior of metallic alloys [J]. Transactions of Nonferrous Metals Society of China, 2017, 27: 2443−2453.

[36] BALLAT-DURAND D, BOUVIER S, RISBET M, PANTLEON W. Multi-scale and multi-technic microstructure analysis of a linear friction weld of the metastable-β titanium alloy Ti−5Al−2Sn−2Zr−4Mo−4Cr (Ti17) towards a new post-weld heat treatment [J]. Materials Characterization, 2018, 144: 661−670.

[37] BACZYNSKI J, JONAS J J. Texture development during the torsion testing of α-iron and two IF steels [J]. Acta Materialia, 1996, 44: 4273−4288.
[38] LI S Y, BEYERLEIN I J, BOURKE M A M. Texture formation during equal channel angular extrusion of fcc and bcc materials: Comparison with simple shear [J]. Materials Science and Engineering A, 2005, 394: 66−77.
[39] FONDA R W, KNIPLING K E. Texture development in near-α Ti friction stir welds [J]. Acta Materialia, 2010, 58: 6452−6463.
[40] WANG Xin-yu, LI Wen-ya, YE Qing, YANG Xia-wei, MA Tie-jun, VAIRIS A. Linear friction welding of a beta titanium alloy: Experimental investigations on microstructure evolution and mechanical properties [J]. Science and Technology of Welding and Joining, 2020, 25: 625−636.
[41] GUO Zhen-guo, MA Tie-jun, LI Wen-ya, ZHANG Yong, ZHAO Zhi-peng, TAO Jun, KANG Wen-jun. Intergrowth bonding mechanism and mechanical property of linear friction welded dissimilar near-alpha to near-beta titanium alloy joint [J]. Advanced Engineering Materials, 2021, 23: 2001479.
[42] GUO Zhen-guo, MA Tie-jun, YANG Xia-wei, CHEN Xi, TAO Jun, LI Ju, LI Wen-ya, VAIRIS A. Linear friction welding of Ti60 near-α titanium alloy: Investigating phase transformations and dynamic recrystallization mechanisms [J]. Materials Characterization, 2022, 194: 112424.

近β型钛合金线性摩擦焊接头变形行为及组织演变的热物理模拟

郭震国[1]，马铁军[1]，杨夏炜[1]，李文亚[1]，陶 军[2]，李 菊[2]，Achilleas VAIRIS[1,3]

1. 西北工业大学 凝固技术国家重点实验室，西安 710072；
2. 中国航空制造技术研究院 航空焊接与连接技术航空科技重点实验室，北京 100024；
3. Mechanical Engineering Department, University of West Attica, Athens, 12241, Greece

摘 要：为了更好地理解近β型钛合金线性摩擦焊(LFW)接头的界面连接行为，采用热压缩物理模拟的方法，以TB2近β型钛合金为研究材料，设计符合LFW工艺特点的帽形热压缩试样，在不同下压量、变形温度及应变速率条件下进行热压缩试验，研究热压缩接头的变形行为及组织演变。结果表明，热压缩过程中热压缩接头连接区(BZ)的峰值剪切应力随变形温度的降低及应变速率的增加而增大，接头BZ的宽度随变形温度和应变速率的增加而减小。接头BZ边缘由沿剪切方向变形的晶粒组成，接头BZ中心由细小的等轴再结晶晶粒组成。接头的动态再结晶机制为连续动态再结晶(CDRX)，且CDRX的程度随下压量、变形温度及应变速率的增加而增大。此外，在界面剪切力的作用下接头BZ边缘形成{112}[111]织构，接头BZ中心形成{110}[001]织构。

关键词：线性摩擦焊；TB2近β钛合金；热物理模拟；变形行为；组织演变；织构演变

(Edited by Wei-ping CHEN)